

Chimera states and synchronization in magnetically driven SQUID metamaterials

J. Hizanidis¹, N. Lazarides^{1,2,3}, G. Neofotistos^{1,3}, and G. P. Tsironis^{1,2,3}

¹Crete Center for Quantum Complexity and Nanotechnology, Department of Physics, University of Crete, P. O. Box 2208, 71003 Heraklion, Greece.

²Institute of Electronic Structure and Laser, Foundation for Research and Technology–Hellas, P.O. Box 1527, 71110 Heraklion, Greece.

³National University of Science and Technology MISiS, Leninsky prosp. 4, Moscow, 119049, Russia

the date of receipt and acceptance should be inserted later

Abstract. One-dimensional arrays of Superconducting QUantum Interference Devices (SQUIDs) form magnetic metamaterials exhibiting extraordinary properties, including tunability, dynamic multistability, negative magnetic permeability, and broadband transparency. The SQUIDs in a metamaterial interact through non-local, magnetic dipole-dipole forces, that makes it possible for multiheaded chimera states and coexisting patterns, including solitary states, to appear. The spontaneous emergence of chimera states and the role of multistability is demonstrated numerically for a SQUID metamaterial driven by an alternating magnetic field. The spatial synchronization and temporal complexity are discussed and the parameter space for the global synchronization reveals the areas of coherence-incoherence transition. Given that both one- and two-dimensional SQUID metamaterials have been already fabricated and investigated in the lab, the presence of a chimera state could in principle be detected with presently available experimental set-ups.

PACS. XX.XX.XX No PACS code given

1 Introduction

Superconducting QUantum Interference Device (SQUID) metamaterials are superconducting artificial media whose function relies both on their geometry and the extraordinary properties of superconductivity and the Josephson effect [1, 2]. Recent experiments on one- and two-dimensional radio-frequency (rf) SQUID metamaterials have revealed their wide-band tuneability, significantly reduced losses, dynamic multistability, and tunable broadband transparency [2, 3, 4, 5, 6, 7]. The simplest version of an rf SQUID involves a superconducting ring interrupted by a Josephson junction [8] (Fig. 1a); this device is a highly nonlinear resonator with a strong response to applied magnetic fields. SQUID metamaterials exhibit peculiar magnetic properties such as negative diamagnetic permeability, predicted both for the quantum [9] and the classical [10] regime. The applied alternating fields induce (super)currents in the SQUID rings, which are therefore coupled through dipole-dipole magnetic forces. This interaction is weak due to its magnetic nature. However, it couples the SQUIDs non-locally since it falls-off as the inverse cube of their center-to-center distance.

Nonlocal coupling in systems of interacting oscillators is capable of producing counter-intuitive space-time patterns, called chimera states [11, 12]. Chimera states are characterized by the coexistence of synchronous and asynchronous clusters of oscillators. They were first observed

over a decade ago, in systems of identical phase oscillators with symmetric coupling [11, 12], and have been intensively studied both theoretically [13, 14, 15, 16, 17, 18, 19, 20, 21, 22, 23, 24, 25, 26] and experimentally, in chemical [27], optical [28], mechanical [29], electronic [30], and electrochemical [31, 32] oscillator systems (for further reading refer to [33]). Recent works also report on the issue of robustness of chimera states [34] as well as on the emergence of chimera states in systems with global [35] and local coupling schemes [36]. Chimera-like states in modular networks [37, 38] have also been investigated, expanding our understanding on the role of topology and dynamics for their occurrence. Recent research efforts aim to stabilize chimera states by feedback schemes [39] and to control the localization of the different regimes [40, 41]. In [42], chimera states with very long life-times were numerically demonstrated in SQUID metamaterials with weak dissipation and non-local magnetic interactions due to an alternating external magnetic field. The SQUID metamaterial model had been previously used in the weak and nearest neighbor coupling regime, for the investigation of intrinsic localization and tuneability effects [43, 44, 45]. Moreover, the synchronization and metastability levels of the chimera states were discussed in terms of appropriate measures [42].

In the present work we extend this study and focus on the multistability of the system where different patterns coexist. Chimera states with single and multiple coher-

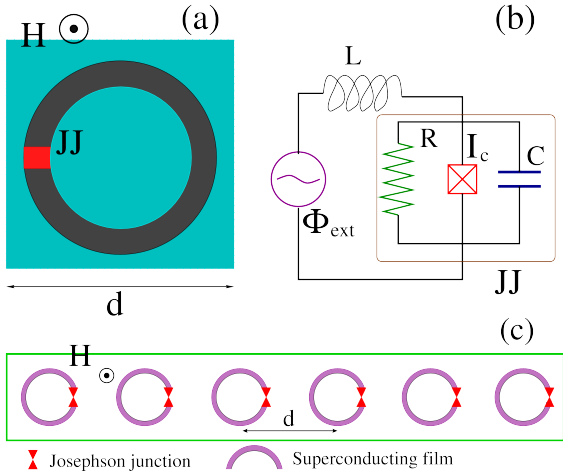


Fig. 1. (Color online) Schematic of an rf SQUID in an alternating magnetic field $\mathbf{H}(t)$ (a), and equivalent electrical circuit (b). The real Josephson junction is represented by the circuit elements that are in the brown-dashed box. (c) A one-dimensional SQUID metamaterial is formed by repetition of the squared unit cell of side d shown in (a).

ent regions of different sizes as well as other patterns will be demonstrated. In addition, by quantifying the spatial synchronization in the SQUID array we reveal the detailed structure of coherence and incoherence in the device. Finally, the parameter space for global synchronization transitions will be analyzed, providing insight into the role of the external driving field. Our results will help to provide further understanding to the implications of the second derivative term (inertia) in the occurrence of chimera states [24, 42, 46, 47], which has not been sufficiently studied.

In the next Section, we present the non-locally coupled SQUID metamaterial model and the measures for quantifying spatial and global synchronization. Current amplitude-driving frequency diagrams for a single SQUID which reveal its multistability property in the strongly nonlinear regime is also presented. In Section 3, the numerically obtained space-time evolution of several coexisting patterns are shown for different initial conditions. The magnitude of the spatial synchronization parameter is monitored in time for the non-locally coupled SQUID metamaterials and the temporal complexity is discussed in terms of phase portraits of the individual SQUID oscillators. In Section 4, the possibility that the SQUID metamaterial may undergo a synchronization-desynchronization transition is explored. Appropriate density plots mapping the order parameter on the dc flux bias - driving period plane unveil the relevant parameter regions in which such a transition may occur. In the concluding section (Section 5) we summarize our results.

2 SQUID Metamaterial Modelling and Measure of Synchronization

The model under consideration involves a one-dimensional linear array of N identical rf SQUIDs coupled together magnetically through dipole-dipole forces. The magnetic flux Φ_n threading the n -th SQUID loop is given by the following equation:

$$\Phi_n = \Phi_{ext} + L I_n + L \sum_{m \neq n} \lambda_{|m-n|} I_m, \quad (1)$$

where the indices n and m run from 1 to N , Φ_{ext} is the external flux in each SQUID, $\lambda_{|m-n|} = M_{|m-n|}/L$ is the dimensionless coupling coefficient between the SQUIDs at positions m and n , with $M_{|m-n|}$ being their corresponding mutual inductance, and

$$-I_n = C \frac{d^2 \Phi_n}{dt^2} + \frac{1}{R} \frac{d\Phi_n}{dt} + I_c \sin \left(2\pi \frac{\Phi_n}{\Phi_0} \right) \quad (2)$$

is the current in the n -th SQUID given by the resistively and capacitively shunted junction (RCSJ) model [48], with Φ_0 and I_c being the flux quantum and the critical current of the Josephson junctions, respectively. Within the RCSJ framework, R , C , and L are the resistance, capacitance, and self-inductance of the SQUIDs' equivalent circuit (Fig. 1b). From Eqs. (1) and (2) we obtain the equation:

$$C \frac{d^2 \Phi_n}{dt^2} + \frac{1}{R} \frac{d\Phi_n}{dt} + \frac{1}{L} \sum_{m=1}^N \left(\hat{\mathbf{A}}^{-1} \right)_{nm} (\Phi_m - \Phi_{ext}) + I_c \sin \left(2\pi \frac{\Phi_n}{\Phi_0} \right) = 0, \quad (3)$$

where $\hat{\mathbf{A}}^{-1}$ is the inverse of the $N \times N$ coupling matrix

$$\hat{\mathbf{A}} = \begin{cases} 1, & \text{if } m = n; \\ \lambda_{|m-n|} = \lambda_0 |m-n|^{-3}, & \text{if } m \neq n, \end{cases} \quad (4)$$

with λ_0 being the coupling coefficient between nearest neighboring SQUIDs.

Normalizing the frequency and time to $\omega_0 = 1/\sqrt{LC}$ and its inverse ω_0^{-1} , respectively, and the fluxes and currents to Φ_0 and I_c , respectively, Eq. (3) reads ($n = 1, \dots, N$)

$$\ddot{\phi}_n + \gamma \dot{\phi}_n + \beta \sin(2\pi \phi_n) = \sum_{m=1}^N \left(\hat{\mathbf{A}}^{-1} \right)_{nm} (\phi_{ext} - \phi_m) \quad (5)$$

where the overdots denote derivation with respect to the normalized temporal variable, τ , $\phi_{ext} = \phi_{dc} + \phi_{ac} \cos(\Omega\tau)$, with ϕ_{dc} being the dc flux component, $\Omega = \omega/\omega_0$ the normalized driving frequency, and

$$\beta = \frac{I_c L}{\Phi_0} = \frac{\beta_L}{2\pi}, \quad \gamma = \frac{1}{R} \sqrt{\frac{L}{C}}, \quad (6)$$

is the SQUID parameter and loss coefficient, respectively.

The corresponding single SQUID equation is obtained from Eq. (5) for $\lambda_0 = 0$, so that $\hat{\mathbf{A}} = \hat{\mathbf{A}}^{-1} = \mathbf{I}_N$, where \mathbf{I}_N

is the $N \times N$ unit matrix, and by dropping the subscript n , as

$$\ddot{\phi} + \gamma \dot{\phi} + \phi + \beta \sin(2\pi\phi) = \phi_{dc} + \phi_{ac} \cos(\Omega\tau). \quad (7)$$

The current I in the SQUID ring is given by the flux-balance condition [45]

$$\phi = \phi_{ext} + \beta i, \quad (8)$$

where $i = I/I_c$. For fixed rescaled SQUID parameter β , the nonlinear effects become stronger with increasing amplitude of the ac field, ϕ_{ac} . In that case, the current amplitude i_{max} - driving frequency Ω characteristic (resonance curve) becomes strongly hysteretic and several simultaneously stable branches appear. This multistability effect is illustrated in Fig. 2, in which two such characteristics are shown in (a) and (b) for weak and strong nonlinearity, respectively. In Fig. 2(a), the SQUID is close to the linear

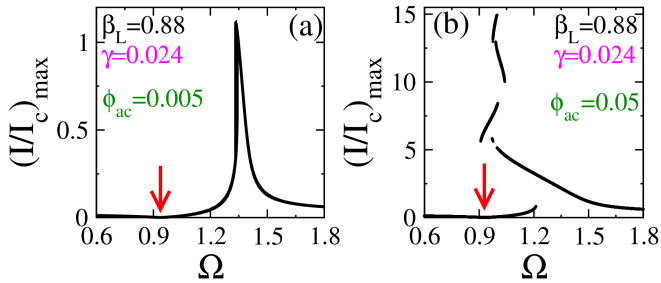


Fig. 2. (Color online) Current amplitude $(I/I_c)_{max}$ - driving frequency Ω characteristics for a single rf SQUID with $\beta_L = 0.88$, $\gamma = 0.024$, $\phi_{dc} = 0$, and (a) $\phi_{ac} = 0.005$; (b) $\phi_{ac} = 0.05$. The red arrows indicate the position of an anti-resonance (see text).

regime, in which the resonance curve is single-valued, in the sense that each value of Ω corresponds to only one value of $(I/I_c)_{max}$. Hysteretic effects are not visible, however the curve is not symmetric as it should be in the truly linear regime. Note that from Eq. (7), linearized around $\phi \simeq 0$, we get for the single SQUID resonance frequency the expression $\Omega_{SQ} = \sqrt{1 + \beta_L}$, which gives $\Omega_{SQ} = 1.37$ for the parameters of Fig. 2. In Fig. 2(b), in which the ac field amplitude has been increased by an order of magnitude, strongly nonlinear effects become readily apparent. At least five stable branches can be identified in a narrow frequency region around unity, i.e., around the geometrical (inductive-capacitive, LC) resonance frequency. The upper branches, which are extremely sensitive to perturbations, correspond to very high values of the current amplitude, which leads the Josephson junction of the SQUID to its normal state. Although the “resonance” region in the strongly nonlinear regime has been shifted to the left, as compared with that in the weakly, almost linear regime, the location of the anti-resonance has not been changed. This can be observed clearly in Fig. 3, where the anti-resonance frequency region has been enlarged in both regimes. The current amplitude anti-resonance makes itself apparent as a well defined dip in the characteristics,

with a minimum that almost reaches zero. The effect of anti-resonance has been observed in nonlinearly coupled oscillators subjected to a periodic driving force [49] and in parametrically driven nonlinear oscillators [50]. However, it has never before been observed in a single, periodically driven nonlinear oscillator. The knowledge of the location of anti-resonance(s) as well as the resonance(s) of an oscillator or a system of oscillators, beyond their theoretical interest, they are of importance in device applications. Certainly they have significant implications for the SQUID metamaterials which properties are determined by those of their elements (i.e., the SQUIDs). When the SQUIDs are in an anti-resonant state, in which the induced current is zero, they do not absorb energy from the applied field which can transpass the metamaterial almost unaffected. Thus, in such a state, the SQUID metamaterial is transparent to the applied magnetic flux as has been already observed experimentally [7]. Moreover, since the anti-resonance frequency is not affected by the amplitude of the ac field, the transparency can be observed for a wide range of applied rf flux. In the strongly nonlinear regime, the anti-resonance lies in the multistability region (see Fig. 2b), due to the frequency shift of the SQUID resonance because of the strong nonlinearity. In that case, the transparency of the metamaterial may be turned on and off as it has been already discussed in Ref. [7]. Thus, the concept of the anti-resonance serves for making a connection between an important SQUID metamaterial property and a fundamental nonlinear dynamical property of oscillators.

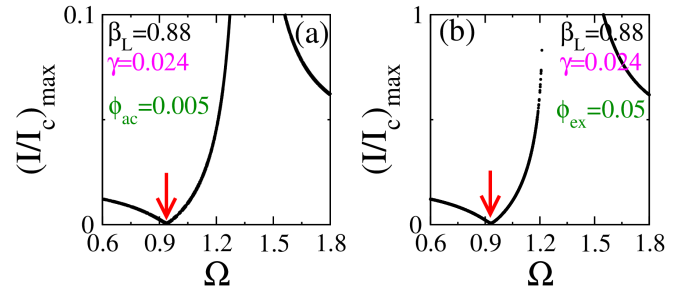


Fig. 3. (Color online) Enlargement of Figs. 2(a) and (b) around the region of the anti-resonance. Same parameters as in Fig. 2.

For the time integration of Eq. (7) of the single SQUID, a fourth-order Runge-Kutta algorithm with constant time-step has been used. The same algorithm is also used for the simulation of the SQUID metamaterial which is modeled by Eq. (5). The latter are implemented with the following boundary conditions

$$\phi_0(\tau) = 0, \quad \phi_{N+1}(\tau) = 0, \quad (9)$$

to account for the termination of the structure in a finite system. The parameter values used in the simulations of the single SQUID and the SQUID metamaterial are in the region in which the relevant experiments were carried out [5, 7]. In Ref. [5], the values of the SQUIDs’ inductance, resistance, and capacitance are $L = 0.12 nH$,

$R = 840 \Omega$, and $C = 0.65 \text{ pF}$, respectively, while the critical current is $3.7 \mu\text{A}$ and $1.2 \mu\text{A}$ at temperature $T = 4.2 \text{ K}$ and 6.5 K , respectively. Inserting these values in the first of Eqs. (6), we get for β_L the values 0.44 and 1.3 at $T = 4.2 \text{ K}$ and 6.5 K , respectively. For the SQUID metamaterial we use $\beta_L = 0.7$, which lies in between those values, while our value of the amplitude of the alternating field $\phi_{ac} = 0.015$ lies within the range of values used in the experiments ($\phi_{ac} \simeq 0.006 - 0.05$). The coupling coefficient between nearest neighbors in Ref. [5] has been estimated to be $\lambda_0 \simeq -0.02$, using a simple approximation scheme in which the SQUIDs are regarded as thin rings. However, a large part of the area of the actual SQUID metamaterial is filled by superconducting material that the field cannot penetrate; it is thus expected that more magnetic flux than that predicted by the simple approximation will find its way through the SQUID rings, increasing thus considerably λ_0 (we use $\lambda_0 = -0.05$). The value of the loss coefficient in our simulations for the SQUID metamaterial is $\gamma \simeq 0.002$ (for the single SQUID $\gamma \simeq 0.024$), while from the second of Eqs. (6) and the values given in Ref. [5] we get ~ 0.02 . Although the losses in the SQUIDs can be reduced considerably by lowering the temperature without affecting much the critical currents of the junctions, we have checked that chimera states also exist for γ of the order of ~ 0.02 when compensated by a larger ac field amplitude ϕ_{ac} . Note that the parameters used in the simulations of the one-dimensional SQUID metamaterial are compared with those in Ref. [5], in which the experiments have been carried out on two-dimensional arrays, merely to show that these are realistic. In this work, we do not attempt to simulate a particular SQUID metamaterial. Moreover, the dimensionality of the system does not affect significantly the estimation of the parameters that are necessary for the simulations, since they can be estimated either by the individual SQUID properties (i.e., β , γ) or by a pair of SQUIDs (i.e., λ_0).

The spatial coherence and incoherence of the chimera state can be characterized by a real-valued local order parameter [18]

$$Z_n = \frac{1}{2\delta} \sum_{|m-n| \leq \delta} e^{i2\pi\phi_m}, \quad n = \delta + 1, \dots, N - \delta. \quad (10)$$

We use a spatial average with a window size of $\delta = 10$ elements. A local order parameter $Z_n = 1$ indicates that the n_{th} unit belongs to the coherent part of the chimera state, while Z_n is less than 1 for incoherent parts. Note that in our system we have no periodic boundary conditions like in [18]; therefore Eq. 10 holds for the SQUIDs with indices running from $n = \delta + 1, \dots, N - \delta$. For the SQUIDs close to boundaries of the structure, the calculation of the local order parameter is modified as follows: $Z_n = \frac{1}{\delta} \sum_{m=n}^{n+\delta} e^{i2\pi\phi_m}$ for $n = 1, \dots, \delta$ and $Z_n = \frac{1}{\delta} \sum_{m=n-\delta}^n e^{i2\pi\phi_m}$ for $n = N - \delta + 1, \dots, N$. A measure for the synchronization level in the whole metamaterial is given by magnitude of the global Kuramoto order parameter $|\Psi(\tau)|$,

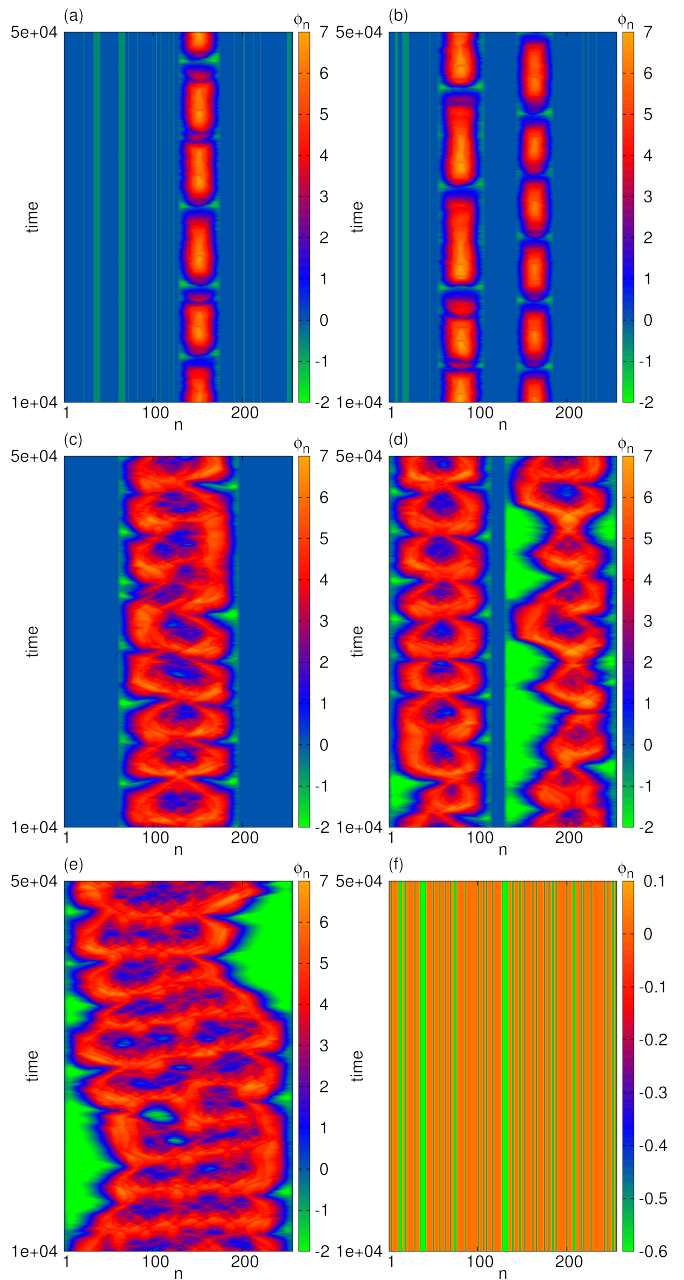


Fig. 4. (Color online) Space-time plots for the flux ϕ_n over the whole SQUID metamaterial for different initial conditions. (a), (c) States with one incoherent region, (b), (d) States with two incoherent regions, (e) Travelling incoherent state, (f) Solitary state. Parameter values are: $T = 5.9$, $N = 256$, $\gamma = 0.0021$, $\lambda_0 = -0.05$, $\beta = 0.1114$ ($\beta_L \simeq 0.7$), $\phi_{ac} = 0.015$, $\phi_{dc} = 0.0$.

where $\Psi(\tau)$ is defined as

$$\Psi(\tau) = \frac{1}{N} \sum_{m=1}^N e^{i[2\pi\phi_m(\tau)]}. \quad (11)$$

This measure will be used in Sec. 4 where the transition from global synchronization to desynchronization will be discussed.

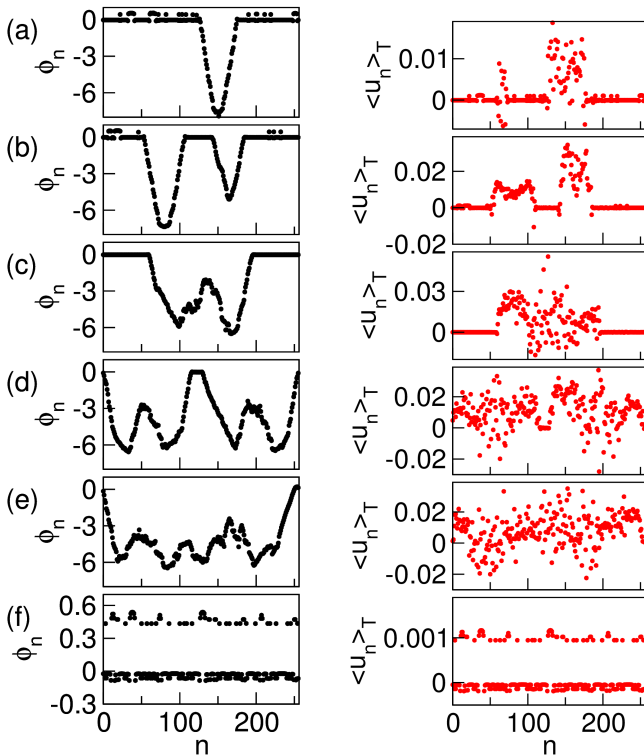


Fig. 5. (Color online) Snapshots of the spatial profile of the fluxes ϕ_n corresponding to Fig. 4 (left panel) and derivative of the phases $\dot{\phi}_n$ averaged over one period of the driving force T . Parameters as in Fig. 4.

3 Multistability and Synchronization

The individual SQUID is a highly nonlinear oscillator exhibiting multistability in a certain parameter regime. This is very crucial for the occurrence of the chimera states when considering the coupled system under investigation. The number of possible states in a SQUID metamaterial is not merely the sum of the combinations of individual SQUID states, since their collective behavior may provide many more possibilities. Depending on the choice of initial conditions, various space-time flux patterns may be obtained, shown in Fig. 4, where the evolution of the ϕ_n s is monitored at times equal to multiples of one driving period $T = 2\pi/\Omega$. In particular, Fig. 4(a) corresponds to a typical pattern with two distinct domains: a cluster of SQUIDS located around $n = 150$ in which the fluxes oscillating with high amplitude coexists with the rest of the array which oscillates with low-flux amplitude. The latter part of the array is not completely homogeneous since small clusters and individual SQUIDS perform slightly higher amplitude oscillations, which manifest themselves through the thin light green lines. In Fig. 4(b) a similar pattern with two clusters of high amplitude oscillations is depicted. Single and double-headed chimera states with larger sizes of incoherent clusters may also be achieved, as shown in Fig. 4(c) and (d), respectively. A coexisting traveling pattern can be seen in Fig. 4(e), where the largest part of the metamaterial is occupied by an incoherent cluster with varying size and position in time. Finally Fig. 4(f) demonstrates

a pattern of low-amplitude oscillations with multiple so-called solitary states [51], where many SQUIDS have escaped from the main synchronized cluster and perform oscillations of slightly higher amplitudes (depicted by the light green stripes in the otherwise orange background).

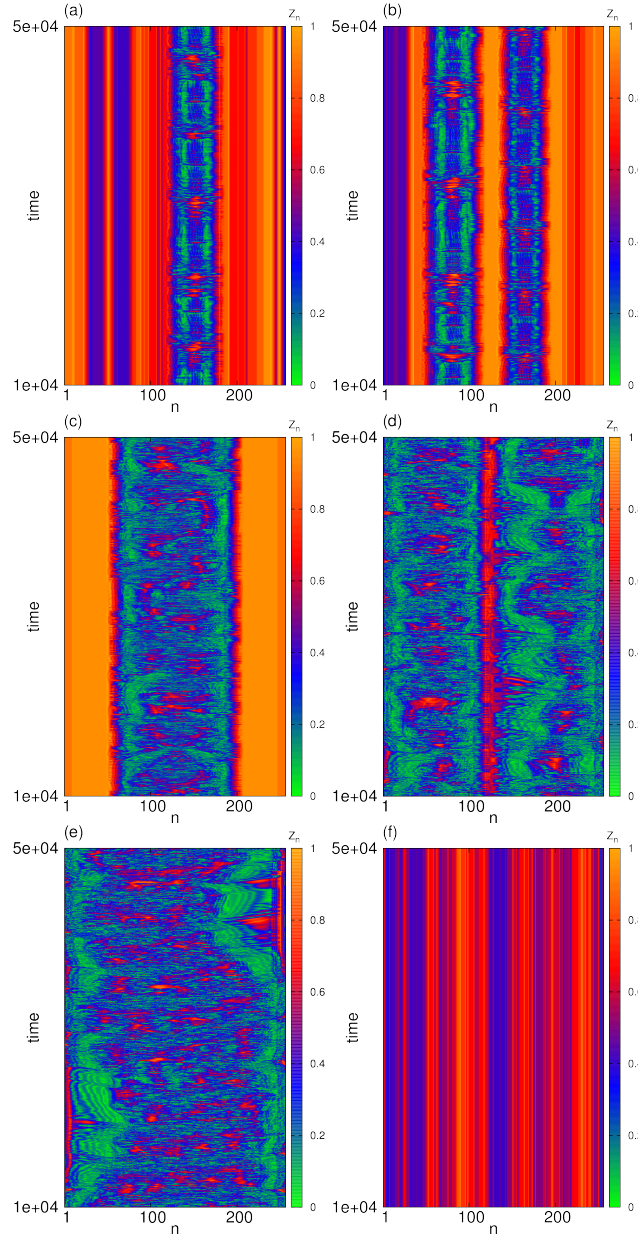


Fig. 6. (Color online) Space-time plots for magnitude of the local order parameter $|Z_n|$ of the corresponding states of Figure 4. Parameters as in Fig. 4.

The corresponding snapshots of ϕ_n and the time-derivatives of the fluxes averaged over T , $\langle \dot{\phi}_n(\tau) \rangle_T \equiv \langle v_n(\tau) \rangle_T$, at the end of the integration time ($\sim 5 \times 10^4$ time units) are shown in the left and right panels of Figs. 5, respectively. Note that $v_n(\tau)$ is the instantaneous voltage across the Josephson junction of the n -th rf SQUID. From the profiles of $\langle v_n(\tau) \rangle_T$ it can be seen that the coherent nodes

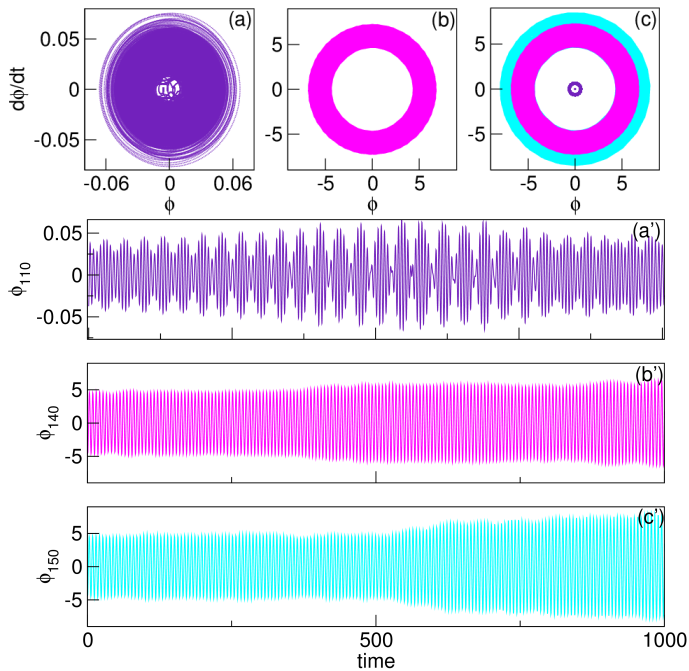


Fig. 7. (Color online) Upper panel: phase portraits of SQUID oscillators at nodes 110 (a); 140 (b); 150 (c). Lower panel: Corresponding time series of magnetic flux ϕ . Parameters as in Fig. 4.

have values very close to zero, which means that the SQUIDS in the coherent part are dominated by the driving force, while the incoherent nodes exhibit small deviations around the external driving frequency. The synchronization within the aforementioned states can be visualized through the space-time plots of the local order parameter (Eq. 10), shown in Fig. 6. Red-orange colors denote the coherent regions and blue-green colors the incoherent ones. These plots reveal the complexity of the synchronization levels in the SQUID metamaterial: For example in Fig. 6(a) it can be seen that the incoherent region located in the center of the system *periodically* achieves high values of synchronization demonstrated by the orange “islands” within the cluster. This is related to metastability, which was extensively studied in [42]. In the coherent cluster, on the other hand, we observe blue stripes of low synchronization which are evident for solitary states that have escaped. Note that *periodic synchronization*, characterized by periodic variation of the order parameter, has been previously observed in phase oscillator models with external periodic driving both with and without an inertial term [52,53].

As already pointed out, a very crucial element for the formation of chimera states in our system is the multistability of periodic solutions in the single SQUID. For a certain set of parameter values, the single SQUID may reach either a high or a low flux amplitude state, from basins of attraction typically smaller in the first case. Nonlocal coupling of SQUIDS can lead to stabilization of high flux amplitude states coexisting with low flux amplitude ones. Typical phase portraits and the corresponding time series for such periodic solutions are shown in Fig. 7 for three

SQUID oscillators of Fig. 4(a). Figure 7(a) corresponds to the SQUID at node 110 which belongs to the coherent cluster of the chimera states of Fig. 4(a), while Figs. 4(b) and (c) refer to nodes on the incoherent cluster, showing high amplitude oscillations. The corresponding time series in Fig. 7(a’)-(c’) show highly modulated quasiperiodic behavior. Additional investigations have shown evidence of chaotic dynamics which requires further study beyond the scope of this paper.

4 Synchronization-desynchronization transition

In the previous sections we have seen how chimera states occur as a result of the high multistability in the SQUID metamaterial. Moreover, it has been demonstrated that the external driving field dominates the frequency of the oscillations and therefore the level of synchronization in the entire device. The external driving field has three control parameters, which would be easily accessible in an experiment: the dc (ϕ_{dc}) and ac (ϕ_{ac}) flux components and the driving period T or equivalently the driving frequency Ω . In Fig. 8 the magnitude of the global order parameter (Eq. 11) averaged over the driving period $T = 2\pi/\Omega$ is shown, in the parameter space of the ϕ_{dc} and T , for three different values of ϕ_{ac} . For very low values of ac component (Fig. 8(a)) the level of synchronization is relatively high in the whole parameter space with distinct spots of lower coherence illustrated by their corresponding red color. Increasing ϕ_{ac} to the value used in the previous sections (Fig. 8(b)), we observe that for $T < 6$ the device is almost always synchronous. Above this critical value an area of desynchronization is formed, including within it a smaller “island” of high synchronization. The blue colored thin areas mark the border between synchronization and desynchronization. Note that the values for which chimera states were found in the previous sections ($T = 5.9$ and $\phi_{dc} = 0$) the system finds itself in an area very close to this transition, which intuitively is logical. For further increase of the ac component (Fig. 8(c)) the synchronization areas shrink while the regions with less and lower coherence become larger. This is interesting because it shows that even though the driving field is stronger, it doesn’t necessarily force all the SQUID oscillators to synchronize. In any case, the order parameter cannot be zero, except in the thermodynamic limit; for a finite system such as the SQUID metamaterial considered here, the order parameter will reach a lower bound in the desynchronized state that depends on the size of the system N . Density plots like those shown in Fig. 8 may be useful for the construction of devices like parametric amplifiers that incorporate SQUID metamaterials [54,55] for which it is essential to avoid all types of noise, chaos, etc.

5 Conclusions

It has been demonstrated that single and double-headed chimera states coexist with solitary states and patterns

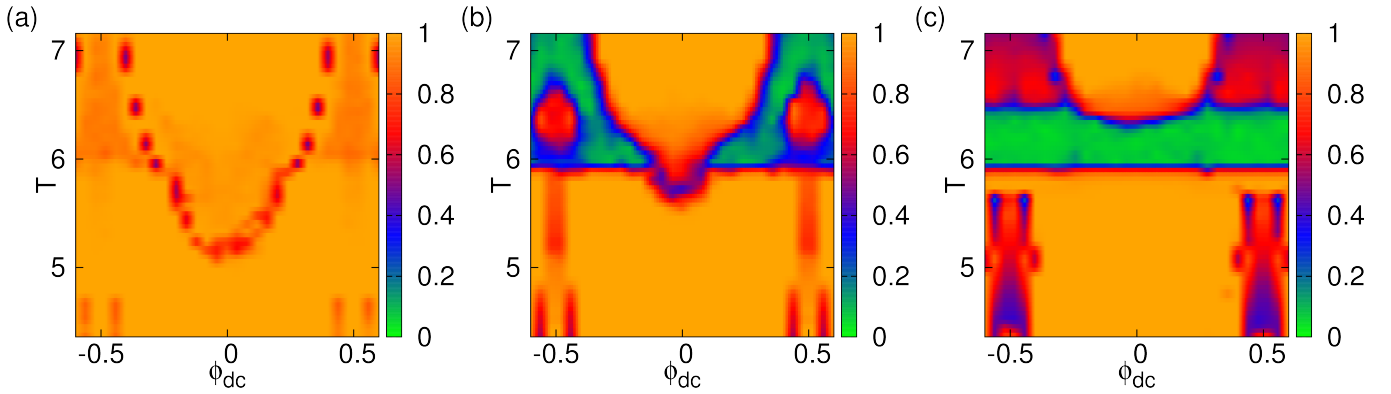


Fig. 8. (Color online) The magnitude of the synchronization parameter (Eq. 11) in the parameter space (T, ϕ_{dc}) , where the brackets indicate averaging over the driving period $T = 2\pi/\Omega$, with Ω being the normalized driving frequency. (a) $\phi_{ac} = 0.003$, (b) $\phi_{ac} = 0.015$, and (c) $\phi_{ac} = 0.05$. Other parameters as in Fig. 4.

of travelling incoherence in nonlocally coupled SQUID metamaterials. These coexisting patterns are a result of the high multistability of the individual SQUID oscillator which tenders the dynamics even more complex when we consider an array of coupled elements. The spatial coherence was calculated through a local order parameter which reveals that the incoherent cluster periodically becomes coherent, a sign of metastability previously studied.

Apart from the spatial complexity with coexisting high and low-flux amplitude oscillators, the dynamics of the coupled system exhibit also temporal complexity. This is demonstrated through the phase portraits and time series of the individual SQUID oscillators, which present a highly modulated quasiperiodic behavior. Evidence of chaos requires further studies which will be included in a future publication. Finally, by scanning the control parameter space of the external dc driving field and the driving period for various values of the ac field amplitude, we were able to locate the regions where the transition from coherence to incoherence occurs. This is relevant for locating chimera states in the available parameter space which may also be useful in device applications.

Our numerical simulations rely on a realistic model, which is capable of reproducing several experimental findings such as the tunability patterns of two-dimensional SQUID metamaterials which are obtained by varying an applied dc flux and the driving frequency [56]. Since several experiments in one- and two-dimensional SQUID metamaterials have been already carried out, revealing very interesting properties peculiar to them, we believe that chimera states could in principle be detected with the presently available set-ups. Thus, SQUID metamaterials may serve as a prototype, test-bed system to check and/or confirm theories and concepts of nonlinear dynamics of coupled oscillators.

Acknowledgements

This work was partially supported by the European Union Seventh Framework Programme (FP7-REGPOT-2012-2013-1) under grant agreement no 316165, the Ministry of Education and Science of the Russian Federation in the framework of the Increase Competitiveness

Program of NUST “MISiS” (No. K2-2015-007), and the Thales Project MACOMSYS, cofinanced by the European Union (European Social Fund ESF) and Greek national funds through the Operational Program “Education and Lifelong Learning” of the National Strategic Reference Framework (NSRF) Research Funding Program: THALES Investing in Knowledge Society via the European Social Fund.

References

1. S. M. Anlage, *J. Opt.* **13**, 024001 (2011).
2. P. Jung, A. V. Ustinov, and S. M. Anlage, *Supercond. Sci. Technol.* **27**, 073001 (2014).
3. P. Jung, S. Butz, S. V. Shitov, and A. V. Ustinov, *Appl. Phys. Lett.* **102**, 062601 (2013).
4. S. Butz, P. Jung, L. V. Filippenko, V. P. Koshelets, and A. V. Ustinov, *Opt. Express* **21**, 22540 (2013).
5. M. Trepanier, D. Zhang, O. Mukhanov, and S. M. Anlage, *Phys. Rev. X* **3**, 041029 (2013).
6. P. Jung, S. Butz, M. Marthaler, M. V. Fistul, J. Leppäkangas, V. P. Koshelets, and A. V. Ustinov, *Nat. Commun.* **5**, 3730 (2014).
7. D. Zhang, M. Trepanier, O. Mukhanov, and S. M. Anlage, *Phys. Rev. X* **5**, 041045 (2015).
8. B. Josephson, *Phys. Lett. A* **1**, 251 (1962).
9. C. Du, H. Chen, and S. Li, *Phys. Rev. B* **74**, 113105 (2006).
10. N. Lazarides and G. P. Tsironis, *Appl. Phys. Lett.* **90**, 163501 (2007).
11. Y. Kuramoto and D. Battogtokh, *Nonlinear Phenom. Complex Syst.* **5**, 380 (2002).
12. D. M. Abrams and S. H. Strogatz, *Phys. Rev. Lett.* **93**, 174102 (2004).
13. O. E. Omelchenko, Y. L. Maistrenko, and P. A. Tass, *Phys. Rev. Lett.* **100**, 044105 (2008).
14. D. M. Abrams, R. Mirollo, S. H. Strogatz, and D. A. Wiley, *Phys. Rev. Lett.* **101**, 084103 (2008).
15. A. Pikovsky and M. Rosenblum, *Phys. Rev. Lett.* **101**, 264103 (2008).
16. E. Ott and T. M. Antonsen, *Chaos* **19**, 023117 (2009).
17. A. Martens, C. R. Laing, and S. H. Strogatz, *Phys. Rev. Lett.* **104**, 044101 (2010).

18. I. Omelchenko, Y. Maistrenko, P. Hövel, and E. Schöll, *Phys. Rev. Lett.* **106**, 234102 (2011).
19. N. Yao, Z.-G. Huang, Y.-C. Lai, and Z.-G. Zheng, *Sci. Rep.* **3**, 3522 (2013).
20. I. Omelchenko, O. E. Omel'chenko, P. Hövel, and E. Schöll, *Phys. Rev. Lett.* **110**, 224101 (2013).
21. A. Vüllings, J. Hizanidis, I. Omelchenko, and P. Hövel, *New J. Phys.* **16**, 123039 (2014).
22. J. Hizanidis, V. Kanas, A. Bezerianos, and T. Bountis, *Int. J. Bifurcation Chaos* **24**, 1450030 (2014).
23. A. Zakharova, M. Kapeller, and E. Schöll, *Phys. Rev. Lett.* **112**, 154101 (2014).
24. T. Bountis, V. Kanas, J. Hizanidis, and A. Bezerianos, *Eur. Phys. J.-Spec. Top.* **223**, 721 (2014).
25. A. Yeldesbay, A. Pikovsky, and M. Rosenblum, *Phys. Rev. Lett.* **112**, 144103 (2014).
26. J. Hizanidis, E. Panagakou, E. Schöll, P. Hövel, and A. Provata, *Phys. Rev. E* **92**, 012915 (2015).
27. M. R. Tinsley and K. Showalter, *Nature Phys.* **8**, 662 (2012).
28. A. M. Hagerstrom, T. E. Murphy, R. Roy, P. Hövel, I. Omelchenko, and E. Schöll, *Nature Phys.* **8**, 658 (2012).
29. E. A. Martens, S. Thutupalli, A. Fourrière, and O. Hallatschek, *Proc. Nat. Acad. Sciences* **110**, 10563 (2013).
30. L. Larger, B. Penkovsky, and Y. Maistrenko, *Phys. Rev. Lett.* **111**, 054103 (2013).
31. L. Schmidt, K. Schönleber, K. Krischer, and V. Garc'a-Morales, *Chaos* **24**, 013102 (2014).
32. M. Wickramasinghe and I. Z. Kiss, *PLoS ONE* **8**, e80586 (2013).
33. M. J. Pannagio and D. Abrams, *Nonlinearity* **28**, R67 (2015).
34. I. Omelchenko, A. Provata, J. Hizanidis, E. Schöll, and P. Hövel, *Phys. Rev. E* **91**, 022917 (2015).
35. F. Böhm, A. Zakharova, E. Schöll, and K. Lüdge, *Phys. Rev. E* **91**, 040901(R) (2015).
36. C. Laing, *Phys. Rev. E* **92**, 050904(R) (2015).
37. M. Shanahan, *Chaos* **20**, 013108 (2010).
38. J. Hizanidis, N. E. Kouvaris, G. Zamora-López, A. Díaz-Guilera, and C. G. Antonopoulos, *Sci. Rep.* (2015) (in print).
39. J. Sieber, O. E. Omel'chenko, and M. Wolfrum, *Phys. Rev. Lett.* **112**, 054102 (2014).
40. C. Bick and E. A. Martens, *New J. Phys.* **17**, 033030 (2015).
41. T. Isele, J. Hizanidis, A. Provata, and P. Hövel, *Phys. Rev. E* (2015) (in print).
42. N. Lazarides, G. Neofotistos, and G. P. Tsironis, *Phys. Rev. B* **91**, 054303 (2015).
43. N. Lazarides, G. P. Tsironis, and M. Eleftheriou, *Nonlinear Phenom. Complex Syst.* **11**, 250 (2008).
44. N. Lazarides and G. P. Tsironis, *Proc. SPIE* **8423**, 84231K (2012).
45. N. Lazarides and G. P. Tsironis, *Supercond. Sci. Technol.* **26**, 084006 (2013).
46. P. Jaros, Y. Maistrenko, and T. Kapitaniak, *Phys. Rev. E* **91**, 022907 (2015).
47. S. Olmi, *Chaos* **25**, 123125 (2015).
48. K. K. Likharev, *Dynamics of Josephson Junctions and Circuits*, Gordon and Breach, Philadelphia (1986).
49. P. Wofo, H. B. Fotsin, and J. C. Chedjou, *Physica Scripta* **57**, 195 (1998).
50. S. Chakraborty and A. Sarkar, *Physica D* **254**, 24 (2013).
51. Yu. Maistrenko, B. Penkovsky, and M. Rosenblum, *Phys. Rev. E* **89**, 060901(R) (2014).
52. M. Y. Choi, Y. W. Kim, and D. C. Hong, *Phys. Rev. E* **49**, 3825 (1994).
53. H. Hong, M. Y. Choi, J. Yi, and K.-S. Soh, *Phys. Rev. E* **59**, 353 (1999).
54. M. A. Castellanos-Beltran and K. W. Lehnert, *Appl. Phys. Lett.* **91**, 083509 (2007).
55. M. A. Castellanos-Beltran, K. D. Irwin, G. C. Hilton, L. R. Vale, and K. W. Lehnert, *Nature Physics* **4**, 928 (2008).
56. G. P. Tsironis, N. Lazarides, and I. Margaritis, *Appl. Phys. A* **117**, 579 (2014).